



Saltwater corrosion behavior of cold sprayed AA7075 aluminum alloy coatings



Sieglind Ngai^{a,b}, Tungwai Ngai^a, Florian Vogel^{b,c}, William Story^b, Gregory B. Thompson^b, Luke N. Brewer^{b,*}

^a School of Mechanical and Automobile Engineering, South China University of Technology, 510640, PR China

^b Department of Metallurgical & Materials Engineering, The University of Alabama, Box 870202, Tuscaloosa, AL 35401-0202, USA

^c Technische Universität Berlin, Department of Materials Science and Technology, Hardenberg-Str. 36, 10623 Berlin, Germany

ARTICLE INFO

Keywords:

Aluminum
Corrosion repair
Cold spray deposition
Pitting corrosion

ABSTRACT

Salt water corrosion behavior of cold sprayed AA7075 is examined. Coatings on AA7075-T651 substrates were prepared by cold spraying AA7075 powder using He and N₂ as carrier gases. Severe plastic deformation is only observed in the helium sprayed samples. Electrochemical experiments performed on the coatings reveal inferior corrosion resistance of the nitrogen sprayed samples, although both coatings exhibit lesser corrosion resistance than the AA7075-T651 substrate. The localized corrosion response is qualitatively different between the three materials with large scale pitting in the plate material, limited pitting in the helium sprayed material, and microscale crevice corrosion in the nitrogen sprayed material.

1. Introduction

Cold gas dynamic spray (CGDS) deposition, also known as “cold spray” (CS) or “supersonic particle deposition” (SPD), is actively being used to repair metallic structures. Using a CS process to repair damage or to apply a corrosion resistant layer on an alloy substrate has the potential to reduce the corrosion damage associated with metallic structures, since coatings with very low porosity level, low oxygen content and fine-grained microstructure can be obtained [1–5]. The process is especially suitable for repair of Al alloys and Mg alloys because of the low thermal input of the cold spray process. Much of the early work has been in dimensional restoration from wear and/or corrosion damage, particularly in magnesium castings [2,4,6]. Champagne et al. successfully used CS of pure aluminum to replace corroded material around fasteners in magnesium castings [6]. In more recent work, CS has been applied to the repair of load-bearing structures using AA7075. Jones et al. have reported that SPD can be used to repair corrosion damage in aircraft aluminum alloys, enhancing the fatigue lives of the repaired coupons and structures [4,7]. Despite these successes in using cold spray deposition for repair, the corrosion performance of the repair material itself remains an open question.

Several authors have examined the corrosion performance of cold sprayed aluminum material [8]. Karthikeyan et al. studied the electrochemical characteristics of cold sprayed AA1100 onto an AA1100 substrate using pure He and a mixture of He-20 vol.% N₂ as carrier

gases [9]. They found that both coatings showed better corrosion resistance than the 1100 Al substrate. While the coating processed with pure He showed a higher degree of plastic deformation, which resulted in a denser structure, it also showed a lower corrosion resistance than that of the He-20 vol.% N₂ sprayed coating. They concluded that although both gases can produce coatings that have a better corrosion resistance than the AA1100 substrate, the addition of N₂ to the carrier gas improved the corrosion resistance of the sprayed coating, which was attributed to the lesser amount of plastic deformation in the coating structure when compared to those sprayed with pure He. Tao et al. produced and analyzed cold spray coatings of pure aluminum on magnesium substrates [10]. They noted the small crystallite size (sub-micron) in the cold sprayed coating. Combined with immersion testing and electrochemical measurements, it was hypothesized that the high density and small crystallite size of the coating produced greater corrosion resistance for the cold sprayed coating compared with a commercial purity aluminum substrate.

The corrosion behavior of the high strength aluminum alloy AA7075, produced by CS deposition, needs to be investigated. Despite its high tensile and fatigue strength, corrosion and corrosion-fatigue can limit the service life of the AA7xxx series alloys components in aviation applications. For instance, pitting degrades the fatigue properties of AA7075 significantly [11,12]. The presence of corrosion pits shortened the fatigue crack initiation life by a factor of two to three and decreased the fatigue crack initiation threshold by about 50% [11]. Meydanoglu

* Corresponding author.

E-mail address: lnbrewer1@eng.ua.edu (L.N. Brewer).

Table 1

Quantitative summary of the results of electrochemical corrosion experiment for the AA7075 material in bulk, cold sprayed with nitrogen gas (N-CS) and cold sprayed with helium gas (He-CS). Data for two different types of experiments: Electrochemical corrosion potential (E_{corr}) from potentiodynamic polarization scans (PD) at scan rates of 0.167 mV s^{-1} and the open circuit potential (OCP) from an open circuit setup (OC) after a holding time of 8 ks. All of these values are reported in volts with respect to a silver-silver chloride reference electrode. The values represent averages from three individual measurements with the corresponding standard deviation, else values represent individual measurements.

Exp.	Bulk		N-CS		He-CS	
	0.1 M	0.6 M	0.1 M	0.6 M	0.1 M	0.6 M
E_{corr} (Volts-SSC), PD 0.167 mV s^{-1}	-0.68 ± 0.01	-0.72 ± 0.01	-0.71 ± 0.01	-0.96 ± 0.03	-0.70 ± 0.01	-0.76 ± 0.04
OCP (Volts-SSC), OC 8 ks	-0.69 ± 0.01	-0.72 ± 0.01	–	–	–	–

et al. utilized CS deposition to deposit AA7075 powder and mixtures of AA7075 and B₄C/SiC powders onto AA6061-T6 plates, and they found that the corrosion potential of the coatings was more noble than the plates while their corrosion rates were much higher than that of the substrate indicating that corrosion of the AA7075 coatings started later but propagated faster when compared to the AA6061-T6 substrate [13]. They attributed the faster corrosion kinetics in the coatings to the presence of more active corrosion sites as a result of higher degree of plastic deformation in the coatings.

In this study, we examine the corrosion behavior of cold sprayed AA7075 deposited onto AA7075-T651 plate substrates. We discuss the differences in corrosion response for fully dense deposits versus porous deposits as produced by helium and nitrogen gases, respectively. Corrosion performance is assessed using potentiodynamic, potentiostatic, and pitting experiments. Detailed microstructure analysis is used to reveal the link between corrosion performance and the microstructure of the CS deposited material.

2. Experimental

2.1. Cold spray procedures

Gas dynamic cold spray (GDCS), hereafter referred to as cold spray (CS), was used to prepare the coatings. The coatings were produced from gas-atomized AA7075 powder (Valimet, USA) with an average particle size of $(16.6 \pm 7.1) \mu\text{m}$ deposited onto AA7075-T651 plate substrates using a high pressure CS system (VRC Metal Systems, USA). The powder had a measured bulk composition of Al-5.4Zn-2.25Mg-1.54Cu-0.19Cr-0.13Si-0.02Mn-0.17%Fe (all in weight-percent). The plate had a nominal composition of Al-Zn(5.1-6.1)-Mg(2.1-2.9)-Cu(1.2-2.0)-Cr(0.18-0.28)-Si(0.4 max)-Mn(0.3 max)-Ti(0.2 max)-Fe(0.5 max). The AA7075-T651 plate substrate material will be referred to as “bulk”, and the nitrogen and helium deposited coatings as N-CS and He-CS, respectively. Prior to spraying, the substrates were grit-blasted with 80 grit garnet powder at a 45° angle. In this study, the coatings were either produced with He (at 2.80 MPa and 375 °C measured at the top of the nozzle) to create fully dense materials or with N₂ (at 3.56 MPa and 480 °C) to produce more porous materials. A standoff distance of 20 mm was used in both cases.

2.2. Microstructural characterization

The microstructures of all samples, i.e. the gas atomized powder, the bulk material, the N-CS and the He-CS coatings, were characterized using scanning electron microscopy (SEM) and optical microscopy (OM). Samples suitable for SEM were prepared by standard metallographic techniques. Final polishing was conducted using a colloidal silica suspension ($\sim 0.05 \mu\text{m}$ particle diameter). The AA7075 powder was mounted in epoxy resin at room temperature prior to grinding and polishing. For SEM analysis, a Tescan Lyra 3 XM Focused Ion Beam (FIB)-Field Emission SEM (FESEM) operated at 10 kV was utilized. Energy dispersive spectroscopy (EDS) elemental maps were collected on this same instrument at 15 kV beam voltage using the EDAX Octane Elite silicon drift detector. Each map was collected for 10 frames at a

signal level of approximately 40–55,000 counts per second. For OM analysis a Nikon Model Epiphot 200 was used. Sample hardness was measured by using a Struers Duramin A300 with a load of 1 kg, and the reported hardness values are an average of 10 different tests where the error is the standard deviation.

2.3. Corrosion testing

Corrosion characteristics were determined utilizing electrochemical and immersion experiments. Before each corrosion experiment the samples were ground using a 2000 grit SiC paper under water and then rinsed with distilled water, then ethanol and finally dried.

2.3.1. Electrochemical tests

All electrochemical experiments were carried out in 0.1 M or 0.6 M NaCl solutions (1 l) using a standard three-electrode cell, involving a silver-silver chloride (Ag/AgCl- 4 M KCl solution) reference electrode and a graphite counter electrode. The solution was purged with Ar gas for at least 45 min prior to the experiment for deaeration. Polarization data was collected using a Gamry PCI 4300-33,004 potentiostat. The temperature was actively maintained at 25 °C during all electrochemical experiments. After the samples were kept in the corrosion cell (with NaCl solution) for 5 min, potentiodynamic polarization experiments were conducted with upward potential scans beginning nominally at -30 mV_{OCP} and ending at $+300 \text{ mV}_{OCP}$, with a scan rate of 0.167 mVs^{-1} , following the approach of Morton and Frankel [14]. The values presented in Table 1 are averages from three individual measurements with the corresponding standard deviation, else values represent individual measurements.

2.3.2. Immersion tests

Immersion experiments on the bulk material, the N-CS and the He-CS coating were carried out in a 0.1 M or a 0.6 M NaCl solution, at open circuit conditions, for 7 days at room temperature (23 °C) after which corrosion products were removed by cleaning the samples in 7% HNO₃ solution, following the example by Gupta et al. [15]. Area ratios of microstructural features characteristic for corrosion after immersion tests were measured utilizing the image analysis software VHX-1000, in which a greyscale threshold-based image segmentation method was applied. For threshold based image analysis, the optical micrographs were converted into 8 bit greyscale images (0 = black, 1–254 shades of grey and 255 white). To determine the area affected by pores or pitting, an interval starting from 0 (black) to a user defined value (below 127) was assigned that best represented this region of interest (ROI). To identify the area that was not affected by corrosion, e.g. the cathodic protection zone (CPZ), an interval starting from 255 (white) to a user-defined value (above 127) was assigned that best represented this ROI. When these areas were identified, the remaining fraction of greyscale values (and their associated pixels) were assigned to general corrosion (GC). In this manner, the 8 bit greyscale interval was subdivided into three parts:

1. Pits/pores: 0 to x, with x < 127
2. Not affected area by corrosion/cathodic protection zone: y to 255,

Table 2

Quantitative assessment of corrosion characteristics after immersing the AA7075 material in 0.1 M and 0.6 M NaCl solutions (open circuit immersion for 7 days at room temperature (23 °C)) for the bulk, cold sprayed with nitrogen gas (N₂-CS), and cold sprayed with helium gas (He-CS) materials. The average area ratios of pits/pores, the cathodic protection zone (CPZ) and the general corrosion (GC) was determined. For the bulk condition the balance resembles not corroded surface.

Material	0.1 M			0.6 M		
	Average area ratio			Average area ratio		
	Pit	CPZ	GC	Pit	CPZ	GC
Bulk	0.11 ± 0.04	–	–	0.26 ± 0.16	–	–
N ₂ -CS	0.09 ± 0.02	0.05 ± 0.07	0.86 ± 0.07	0.20 ± 0.05	0.09 ± 0.08	0.71 ± 0.10
He-CS	0.05 ± 0.02	0.15 ± 0.06	0.80 ± 0.09	0.05 ± 0.01	0.15 ± 0.08	0.80 ± 0.10

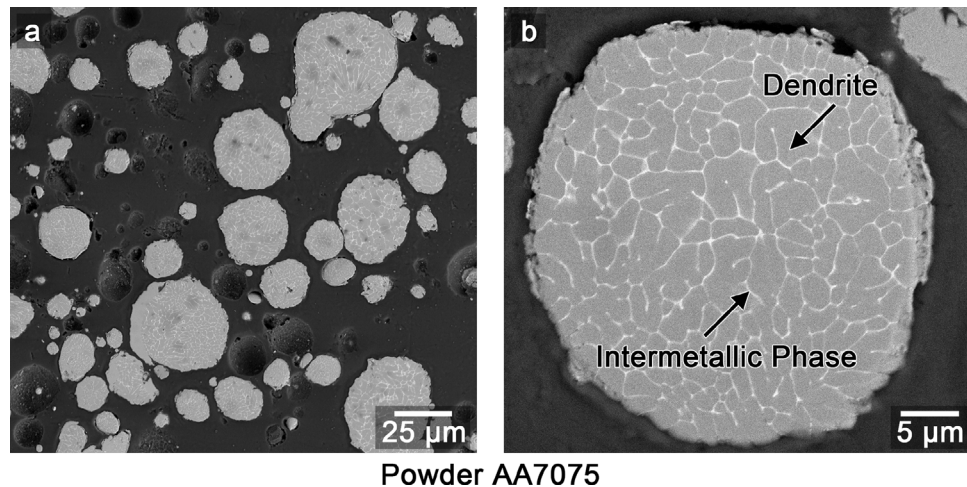


Fig. 1. BSE-SEM micrographs of powder AA7075 in the as-received condition, (a) particle size distribution, (b) cross-section of a typical particle depicting its dendritic microstructure.

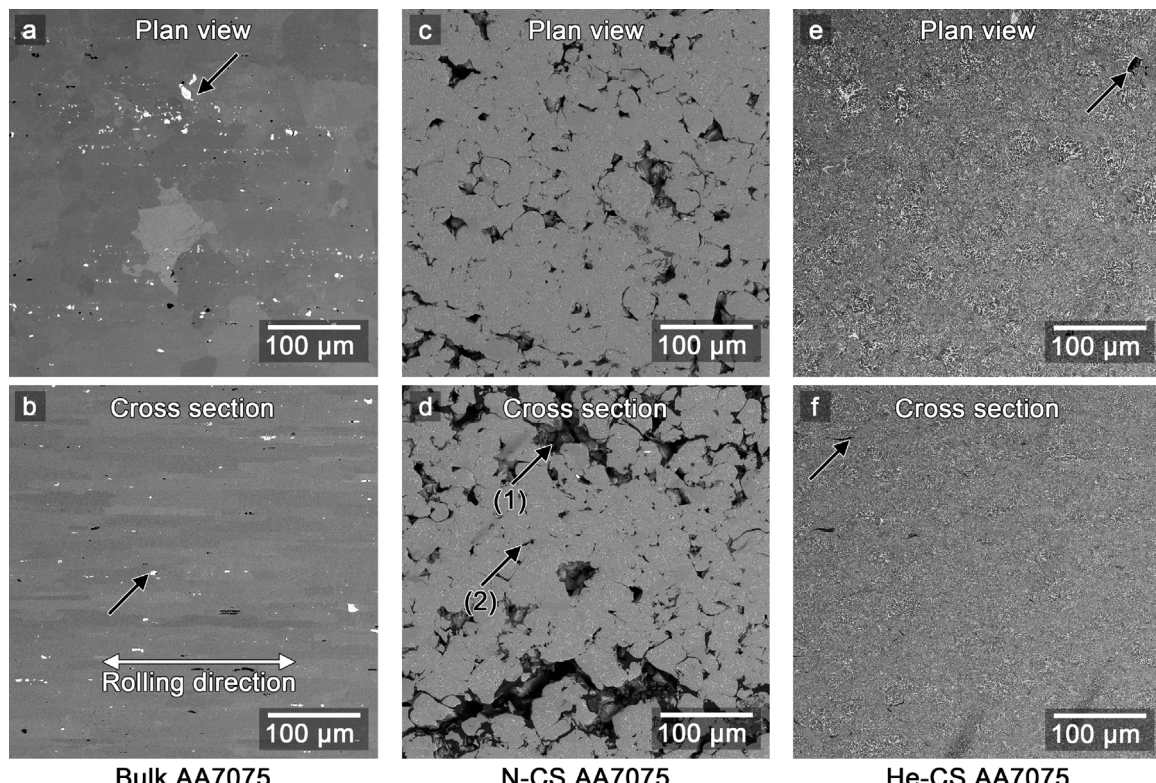


Fig. 2. BSE-SEM micrographs in plan view (top row) (a) bulk, (c) nitrogen cold sprayed (N-CS) and (e) helium cold sprayed (He-CS) and cross section (bottom row) (b) bulk, (d) N-CS and (f) He-CS. Please note: (a and b) Bulk material: constitutive intermetallic particles (bright phase) indicated by arrows. (c and d) N-CS: Heterogeneous microstructure with (1) a network of large pores between two subsequent layers of deposited material and (2) smaller pores distributed within a cold sprayed layer. (e and f) He-CS: Homogeneous microstructure with small, isolated pores shown by arrows.

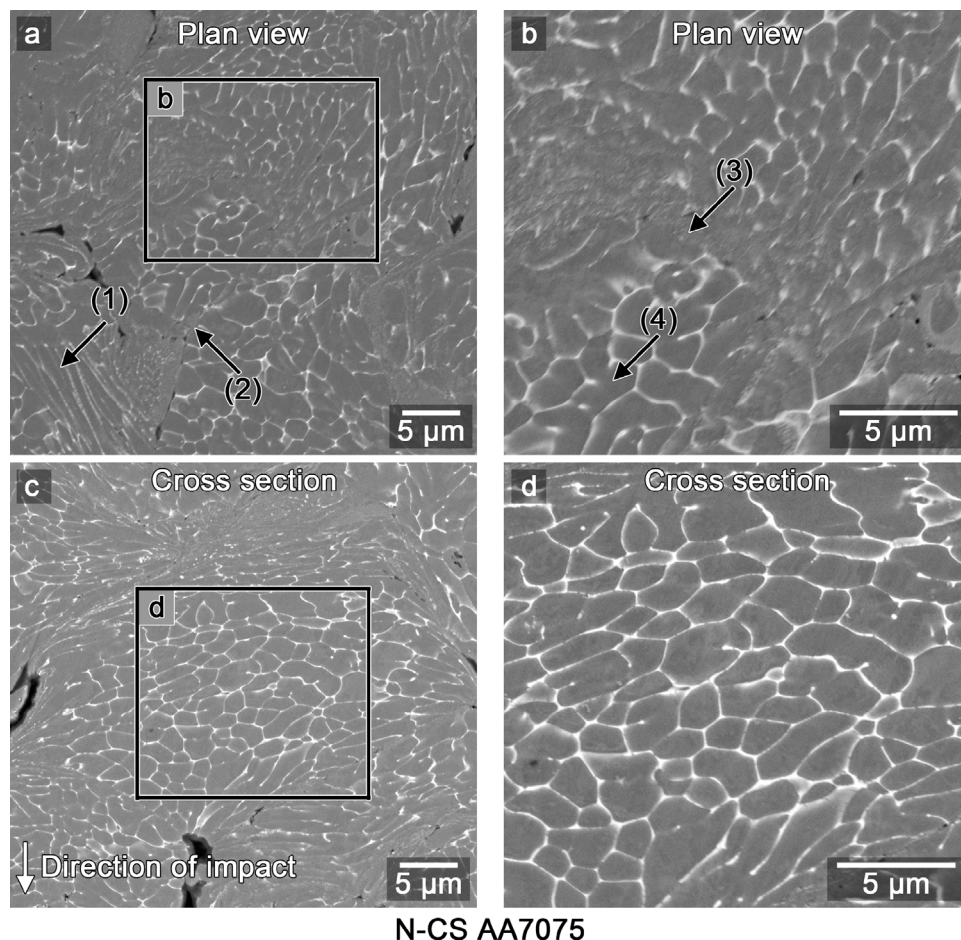


Fig. 3. BSE-SEM micrographs of the microstructure of the AA7075 material in N-CS condition. (a) and (b) show plan view orientation and in (a) plastic deformation is indicated by a refined network of intermetallic phases (indicated by a black arrow (1)) and also junctions between multiple prior particles is visible (indicated by a black arrow (2)). An enlarged view of the black box in (a) is shown in (b) where a highly deformed region and the interior of a particle are indicated by black arrows (3) and (4) respectively. (c) and (d) provide cross section views whereby the interior of a particle marked by a black box is shown at further magnification in (d). In (c) the direction of particle impact during cold spray deposition is indicated.

with $y > 127$

3. General corrosion zone: x to y

Using this approach, the area fraction of each corrosion type was determined and related to the total image area (number of pixels divided by the number of total pixels) in order to determine the values listed in Table 2.

3. Results and discussion

3.1. Microstructural characterization

Fig. 1 shows backscattered electron (BSE)-SEM cross section images of as-atomized powder particles displaying microstructures that would be expected from such a rapid solidification process. The majority of the powder particles are nearly spherical in shape with an average particle size of about $(16.6 \pm 7.1) \mu\text{m}$ (Fig. 1a). a) For a detailed picture of the interior of a powder particle, an enlarged view of a single particle is given in Fig. 1b. The interior is comprised of a dendritic microstructure with clearly visible dendrite cores (grey) and dendrite boundaries (white-grey) at which intermetallic phases have formed. Recent work by Molnárová *et al.* has identified this phase in as-atomized AA7075 powder as the $\text{Mg}_{32}(\text{Zn},\text{Al},\text{Cu})_{49}$ phase, a metastable precursor to the $\text{Mg}(\text{Zn},\text{Al},\text{Cu})_2$ phase that forms in this alloy [16]. Black arrows mark a dendrite core and a region of intermetallic phase. It is important to note that the cold sprayed material microstructure will simply be a deformed version of this initial powder microstructure.

Fig. 2 shows representative plan view (top) and cross section (bottom) BSE-SEM images of the microstructures of the material in (a, b) bulk, (c, d) N-CS and (e, f) He-CS deposited conditions. The

microstructure of the bulk material contains Cu- and Fe-rich constituent particles, such as $\text{Al}_7\text{Cu}_2\text{Fe}$, $\text{Mg}(\text{Zn},\text{Al},\text{Cu})_2$ and Al_3Fe (Fig. 2a and b). These particles are irregular in shape and usually with a size of several microns. In addition, these constituent particles are aligned along lines in the rolling direction, which is also indicated. The $\text{Al}_7\text{Cu}_2\text{Fe}$, $\text{Mg}(\text{Zn},\text{Al},\text{Cu})_2$ and Al_3Fe phases are all cathodic to the aluminum matrix [17,18]. In Fig. 2c and d the microstructure of the N-CS coating, reveals a high level of porosity, particularly pores at junctions between multiple prior particles, resulting from insufficient bonding between some of the initially spherical powder particles. The vast majority of pores in the N-CS coating is interconnected and resembles a network of pores. The deformation of the particles in the less porous regions does not appear to be severe enough to produce a dense coating and many small pores remain in between the deformed particles. The spherical shape of the original powder particles is largely retained, which further indicates a rather low degree of plastic deformation upon particle impact. Thus the resulting microstructure appears non-uniform and it can be distinguished between two different types of pores: (1) a network of large pores and (2) sparsely distributed, small and deformed pores (indicated by black arrows). Thereby, the network of large pores forms between two subsequent layers of CS material. Fe- and Cu-containing aluminide precipitates, commonly observed in AA7075 [19–22], are not observed in this N-CS coating. Fig. 2e and f show the microstructure of the He-CS coating, which in contrast to that of the N-CS coating (Fig. 2c and d), possesses a much more uniform and dense appearance with a very low degree of porosity. Two medium sized blocky pores can be identified in Fig. 2 e and a few very small and elongated pores in Fig. 2f (both indicated by black arrows). The initially spherical morphology of the powder particles is no longer visible, indicating severe plastic deformation after CS deposition.

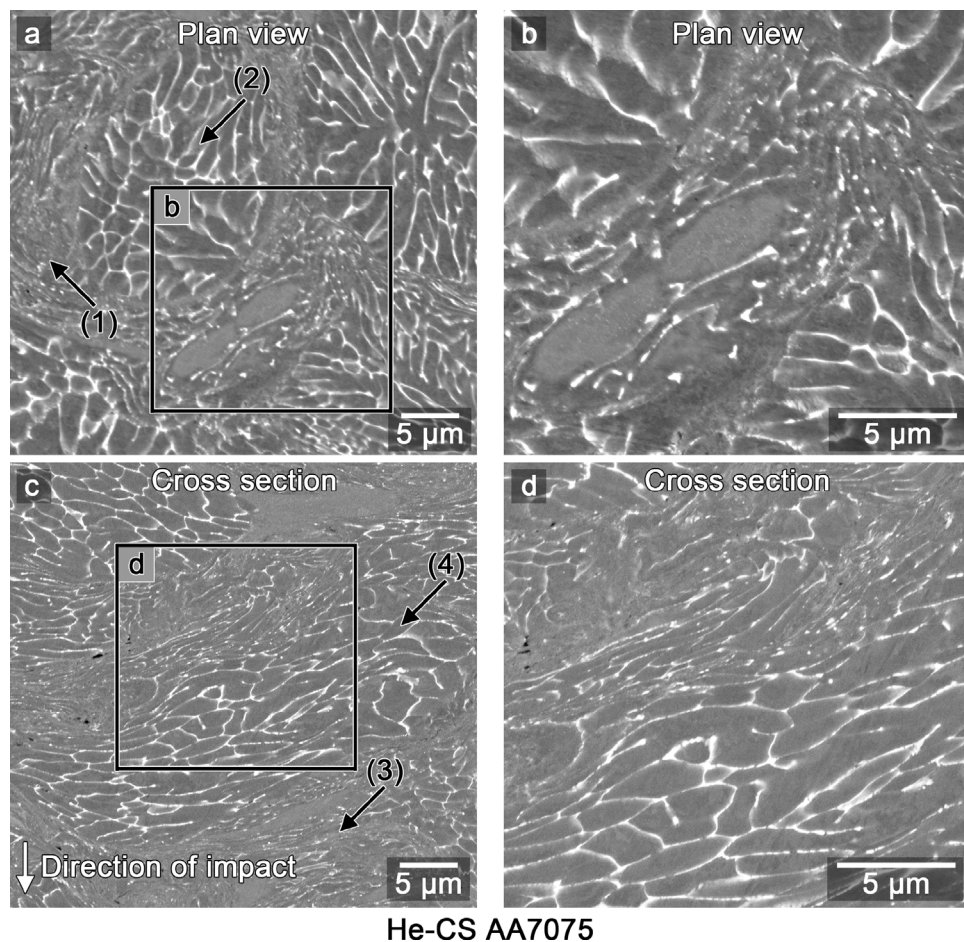


Fig. 4. BSE-SEM micrographs of the microstructure of the AA7075 material in He-CS condition. (a) and (b) show plan view orientation and in (a) plastic deformation is indicated by a refined network of intermetallic phases and indicated by a black arrow (1) whereas the interior of a particle is also indicated by a black arrow (2). An enlarged view of the black box in (a) is shown in (b) where a highly deformed and densified region between three particles is shown. (c) and (d) provide cross section views whereby a highly deformed region between two particles (as marked by a black arrow (3)) and the interior of a particle (as indicated by a black arrow (4)) are marked by a black box and shown at further magnification in (d). In (c) the direction of particle impact during cold spray deposition is indicated.

Fig. 3 provides BSE-SEM images, which give a detailed picture of the N-CS coating microstructure in plan view (Fig. 3a and b, top) and cross section (Fig. 3c and d, bottom) orientations. While the previously shown images of the N-CS coating (Fig. 2b) did not show clear evidence of plastic deformation, images at higher magnification (shown in Fig. 3) show that some of the particles have undergone plastic deformation i.e. elongation, as marked by black arrow (1) in Fig. 3a. Junctions between multiple prior particles can also be observed and are marked by a black arrow (2) in Fig. 3a. In addition, numerous intergranular pores (dark/black) appear deformed between particles. The presence of equiaxed grains near the center of prior particles after deposition indicates insufficient plastic deformation and a lack of bonding among the particles, both due to the impact force being too low. As described earlier (Fig. 2), the solidification cell boundaries of the as-received AA7075 powder show strong segregation of the alloying elements, which in most cases form intermetallic phases at the cell boundaries, potentially affecting the mechanical properties of the material. An even more enlarged view is given in Fig. 3b in which a small degree of plastic deformation can be identified between two particles marked by a black arrow (3). Single, original particles can still be identified based on their non-deformed interior microstructure as marked by a black arrow (4) and also shown in the cross section view at the bottom. In Fig. 3 c, the cross section view reveals a slightly higher degree of plastic deformation in the direction of impact on the substrate as the interior of a previous particle appears compressed. An enlarged view of the slightly deformed interior of this particle is shown in Fig. 3d.

Fig. 4 displays BSE-SEM images providing a detailed picture of the He-CS coating in plan view (Fig. 4a and b, top) and cross section (Fig. 4c and d, bottom) orientation. In keeping with the homogeneous microstructure of the He-CS coating shown in Fig. 2e and f, a higher

magnification view of the corresponding condition (He-CS) (Fig. 4a and b) reveals a large degree of plastic deformation. This substantial plastic deformation is due to the higher impact velocity (kinetic energy) of the powder particles upon CS deposition with He gas as compared to N₂ gas. In contrast to the N-CS microstructure, in Fig. 3a and b the exterior of previous particles is deformed to such a high degree that the region in between is comprised of a refined network of intermetallic phases as indicated by black arrows (1) and (3) in Fig. 4a and c, respectively. Interestingly, when viewed in the plan view orientation, the interior microstructure of the prior particles (Fig. 4a and b) appears to be largely maintained as compared to the powder particles microstructure shown in Fig. 1b. However, in the cross section perspective (Fig. 4c and d) severe plastic deformation is clearly present not only between particles (black arrow (3)) but also in the interior of the particles (black arrow (4)). Further, porosity is not common; only a few sub-micron pores are visible in the cross section view (Fig. 4c and d).

The difference of the N-CS and the He-CS coatings is also reflected by their basic mechanical properties, which were determined by Vickers hardness measurements. The bulk material, with a hardness of (120.5 ± 7.6) HV, shows the same hardness as the N-CS coating with a Vickers hardness of (120.5 ± 11.6) HV. In contrast, the He-CS coating, with (158.8 ± 2.8) HV, reveals a significantly higher hardness. The increased hardness of the He-CS coating versus the bulk material and the N-CS coating can be attributed to microstructural differences in terms of homogeneity, porosity (size and number of pores) and the hardening effect of severe plastic deformation during the CS process as discussed above. The connections between particle velocity and increased particle deformation, plasticity, and hardness have been previously made by several authors [13,23,24].

These microstructural differences are a result of the velocity of the

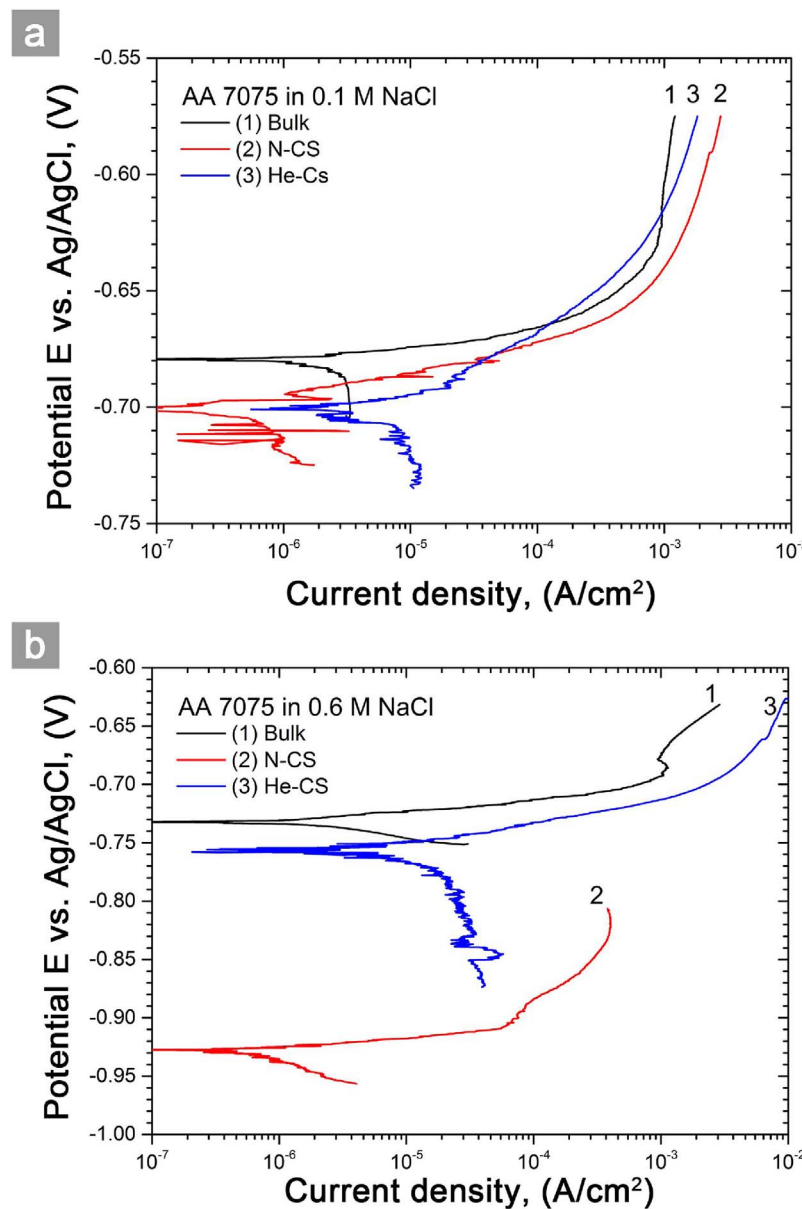


Fig. 5. Corrosion behavior of the AA7075 material in bulk (black-curve 1), N-CS (red-curve 2) and He-CS (blue-curve 3) condition in a solution of (a) 0.1 M and (b) 0.6 M NaCl as determined by potentiodynamic polarization scans.

impacting powder particles during the CS and the subsequent plastic deformation experienced by the particles when impacting the substrate. The impact velocity of the particles is directly related to the ratio of specific heats for the carrier gas, and inversely related to the mass of carrier gas [25]. He possesses a higher ratio of specific heat when compared to N₂, providing more thrust to the powder particles. In addition, the lower density of the He gas increases the velocity of the powder particles thus enhancing integrity and density of the coating. Some of the early cold spray work by Gilmore *et al.* showed that copper particles accelerated by air had a mean particle velocity of 400 m s⁻¹ while the same copper particles accelerated by He gas had a mean particle velocity of 650 m s⁻¹ [26]. Recent work by Ozdemir *et al.* using AA6061 particles in a VRC system very similar to the one in this paper showed a substantial effect from the carrier gas on aluminum particle velocity [27]. The measured mean particle velocity for nitrogen gas is approximately 600 m s⁻¹, while a 70% nitrogen-30% helium gas mixture drives the particles to a mean velocity of 800 m s⁻¹.

3.2. Corrosion behavior

The corrosion behavior was characterized utilizing potentiodynamic

polarization (PD) experiments where a potential was applied and the resulting current density was recorded and immersion experiments without applying or recording a potential and current density. Fig. 5 shows the potential *E* in V vs. an Ag/AgCl electrode as a function of current density *i* for the AA7075 material in bulk (black), N-CS (red) and He-CS (blue) deposited condition. Further, Table 1 quantitatively summarizes the results of the corrosion experiments in terms of *E*_{corr} upon PD scanning with 0.167 mV s⁻¹ and also the OCP upon immersing for 8 ks. Fig. 5a depicts the results of PD experiments in a solution of 0.1 M NaCl. The bulk material exhibits the highest *E*_{corr} of about -0.67 V (SSC) as compared to the N-CS and He-CS coatings, which show the same *E*_{corr} of about -0.70 V. Thus, the tendency of the N-CS and He-CS coatings to corrode is slightly higher. However, within the error there is no significant difference in corrosion potential among these three conditions. For the N-CS and the He-CS coatings, sporadic spikes in the current density for potentials above *E*_{corr}, indicate the onset of pitting. Such spikes are absent for the bulk material, where merely a smooth slope is present. Fig. 5b shows the graphs of PD experiments in a solution of 0.6 M NaCl. Again, the bulk material represents the highest *E*_{corr} with about -0.73 V, slightly more active with the increase in chloride concentration. For the N-CS coating, *E*_{corr} drops

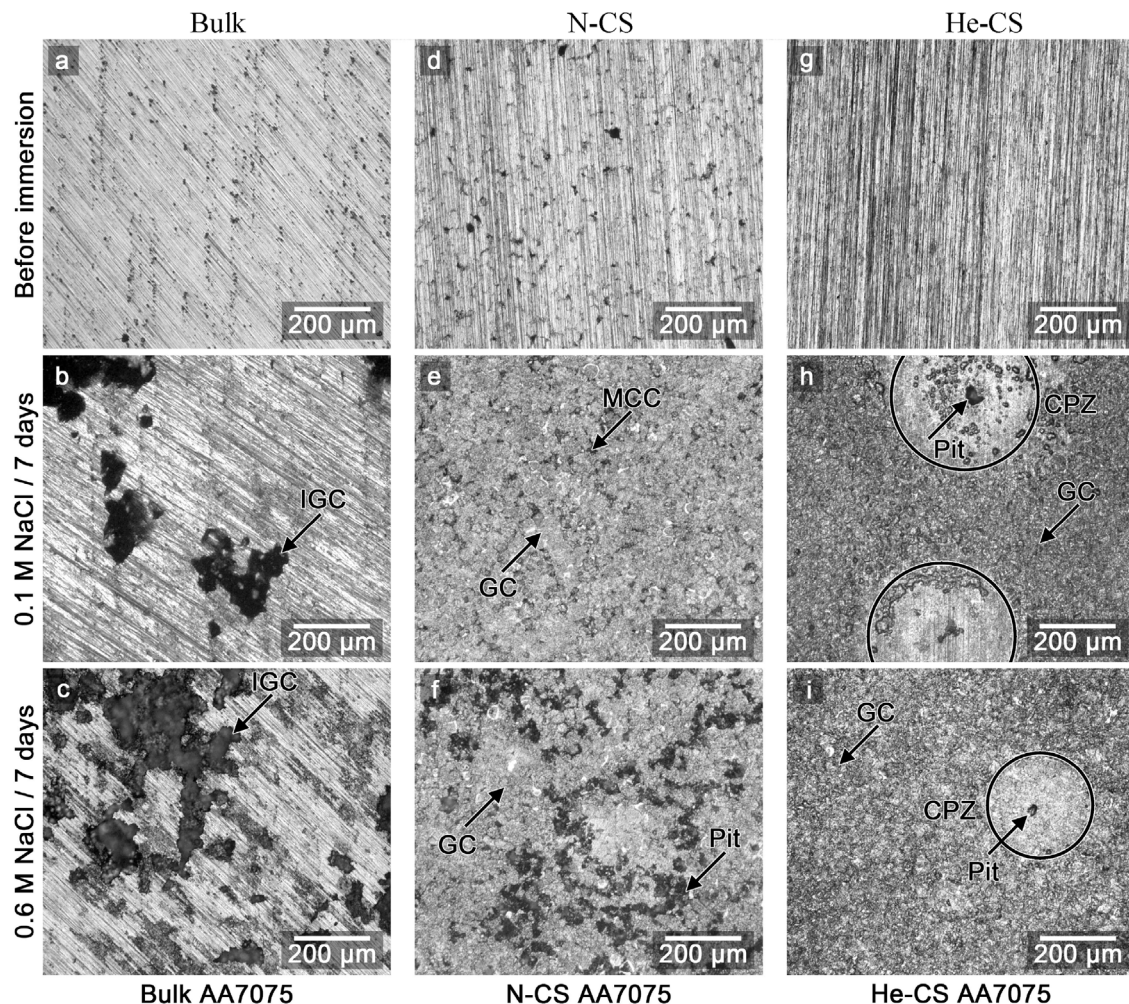


Fig. 6. Optical micrographs of the AA7075 material in bulk (a–c), helium cold sprayed (He-CS) (d–e) and nitrogen cold sprayed (N-CS) (g–i) deposited condition before (top row) and after open circuit immersion in 0.1 M and 0.6 M NaCl for 7 days (middle and bottom row respectively). Pores, pits, intergranular corrosion (IGC), micro crevice corrosion (MCC) and general corrosion (GC) are indicated by black arrows. The cathodic protection zone (CPZ) is marked by a black circle.

to about -0.93 V, which is considerably below E_{corr} of the bulk material. In contrast, E_{corr} for the He-CS coating only drops slightly to about -0.75 V with the increase in chloride concentration. Thereby, the bulk material and the He-CS coating reveal an E_{corr} that is only -0.05 V lower as compared to the 0.1 M NaCl solution. These results indicate that even in a harsher environment more comparable to seawater (0.6 M NaCl) there is not much decrease in corrosion resistance of the He-CS coating as compared to the bulk material. The N-CS material degrades significantly with increasing chloride concentration.

Fig. 6 is a compilation of optical micrographs (OM) of the AA7075-T651 material in bulk (Fig. 6a–c), N-CS (Fig. 6d–f) and He-CS (Fig. 6g–i) as-deposited conditions before (top row) and after (middle and bottom row) immersion in either 0.1 M or 0.6 M NaCl for 7 days. Fig. 7 shows higher magnification, secondary electron images of the corroded surfaces after immersion in 0.6 M NaCl. To quantify the relative contributions of different corrosion types, the average area ratio of pits (black arrows), cathodic protection zones (black circle), and general corrosion are determined by evaluating 11 optical micrographs for each condition. These quantitative results are listed in Table 2.

Before immersion (Fig. 6a) the bulk material reveals scratch marks from sample preparation and stringers of intermetallics aligned along lines in the rolling direction of the plate material (as seen in Fig. 2a and b). In Fig. 6b, after immersing in 0.1 M NaCl for 7 days, the scratch marks are still visible. In addition, relatively large (50–200 μm), irregularly shaped pits are present. These pits are believed to originate from anodic dissolution of the matrix around the constituent particles at

the grain boundaries in the bulk material. Anodic dissolution of the matrix around Cu- and Fe-rich constituent particles has been previously reported for AA7075 [17,18]. This dissolution progresses into intergranular corrosion (IGC, black arrow) and pitting. In Fig. 6c for samples immersed in 0.6 M NaCl the IGC eventually leads to large, irregular shaped pits that follow the contours of the alpha aluminum grains (also see Fig. 7a). As the corrosion proceeds, these pits become interconnected and form networks. Note that the regions between pit networks still show the scratches from sample preparation. These results indicate that for the bulk material, pitting combined with IGC are the dominant corrosion mechanisms since general corrosion (GC) is not evident.

In Fig. 6d, the N-CS coating before corrosion also exhibits scratch marks and exhibits sparsely distributed pores (5–20 μm, black arrow) (cf. Fig. 2c and d). In Fig. 6e, after immersing the N-CS coating in 0.1 M NaCl for 7 days, individual pits or pores cannot be identified, and the scratch marks have all disappeared. Instead, a mixture of micro-crevice and general corrosion (MCC and GC, respectively) is observed, with an obvious dependency on the molarity of the solution. In Fig. 6e, after immersing in 0.1 M NaCl the surface resembles general corrosion while in Fig. 6f, after immersing in 0.6 M NaCl, larger, localized corrosion features can be seen which resemble pits. These features seem to be filled with a corrosion product which is oxygen-rich, most likely an oxide or hydroxide (Figs. 7 b and 8 d–f). We describe this as crevice corrosion on a microscopic scale because the corrosion process is not nucleating any new pits for the N-CS coating. Initially, the N-CS coating

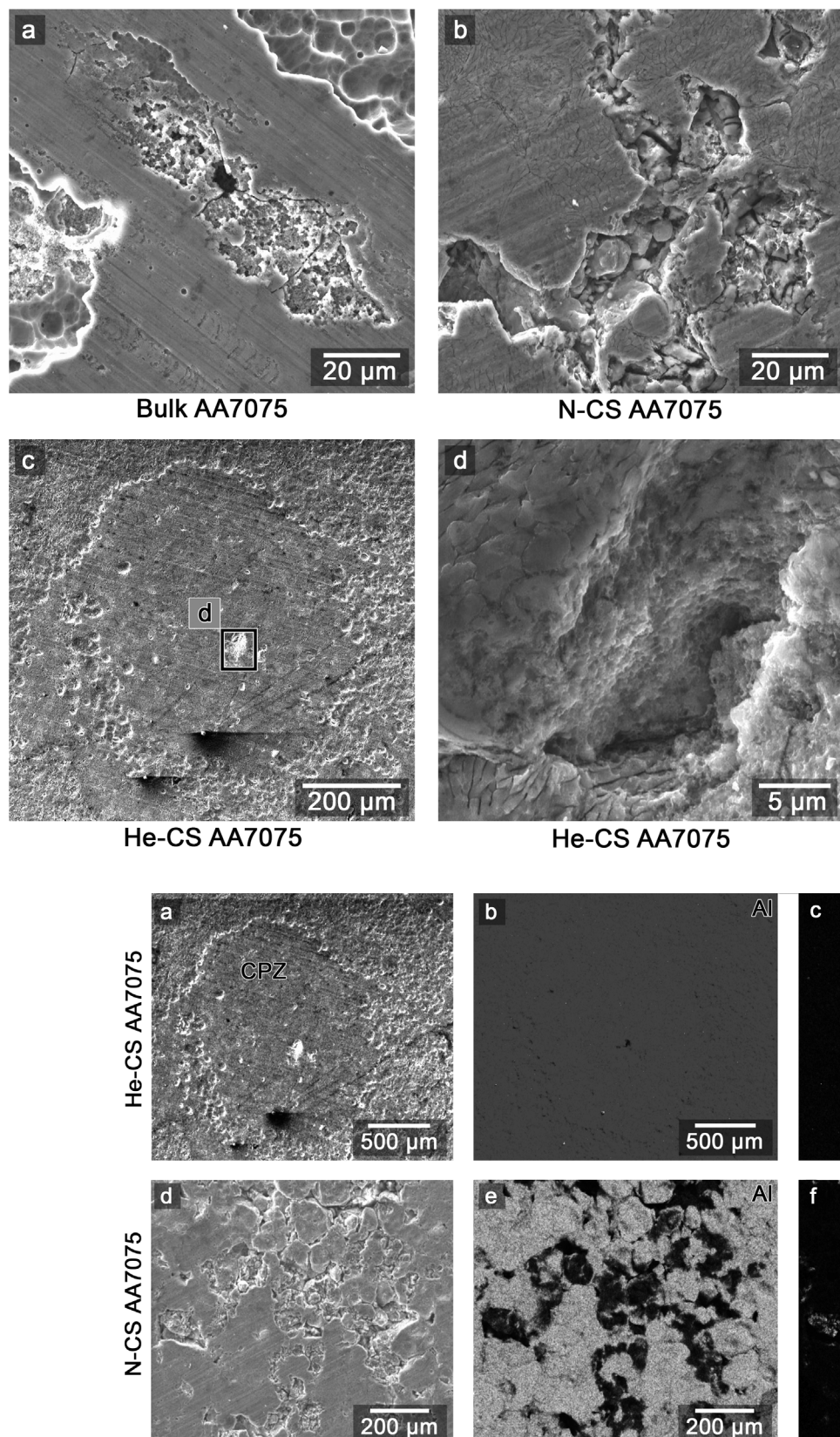


Fig. 7. Detail SEM images of the AA7075 material in bulk (a), nitrogen cold sprayed (N-CS) (b) and helium cold sprayed (He-CS) (c, d) deposited condition after immersion in 0.6 M NaCl for 7 days. The area marked by a black rectangle in (c) is shown with further magnification in (d). All images taken using secondary electrons (SE).

Fig. 8. SEM images and EDS elemental maps of the AA7075 material in helium cold sprayed (He-CS) (a–c) and nitrogen cold sprayed (N-CS) (d–f) deposited condition after immersion in 0.6 M NaCl for 7 days. (a) Secondary electron (SE) image of a cathodic protection zone (CPZ) is indicated and the corresponding Al (b) and O (c) distribution is shown. (d) SE image of corrosion inside pores and the corresponding Al (e) and O (f) distribution is highlighted. EDS elemental maps are shown in greyscale.

shows a relatively high degree of porosity (cf. Fig. 2c and d). Here, the NaCl solution simply penetrates from the surface into the material through these pores and corrosion may proceed. Because these interconnected pores do not have ready access to the surface, the solution can become acidified as corrosion proceeds, thus accelerating it even more. The higher level of Cl⁻ concentration in the 0.6 M NaCl only exacerbates the occluded corrosion and is likely the reason why in the PD polarization scans, the curve for the N-CS coating drops dramatically as the solution is changed from 0.1 M to 0.6 M NaCl (cf. green curve, Fig. 5b).

Before immersion, the He-CS coating (Fig. 6g) only displays scratch marks (cf. Fig. 2e and f). After immersing in 0.1 M NaCl for 7 days, Fig. 6h reveals an entirely different picture when compared to the corresponding corroded surfaces of the bulk and the N-CS coating. Here, noticeable, circular areas form around obvious pits (black arrow) (see also Fig. 7c and d). We describe these areas as cathodic protection zones (CPZs), which are the surface regions required as cathodes to support the anodic dissolution reactions taking place in the pit. While the CPZs appear with diameters of about 150–400 μm, the pits in their center are relatively small (5–20 μm). In the CPZ, corrosion is largely suppressed since the original scratch marks are still slightly visible. Moreover, it appears that in the CPZ at the top in Fig. 6h, additional smaller pits form surrounding the large one in the center. The remaining area in between the CPZs is affected by general corrosion and no scratch marks are visible anymore. Fig. 6i when immersed in 0.6 M NaCl for 7 days, the result is comparable to that of immersing in 0.1 M NaCl. However, the scratch marks on the CPZs marks are less clear when exposed to this higher molarity solution, suggesting that some corrosion has taken place (Fig. 6h). No noticeable changes in elemental composition across the CPZs are noted using EDS elemental mapping after immersion for the helium cold sprayed material (Fig. 8a–c). In contrast, the pit/pore regions in the nitrogen cold sprayed material show a strong oxygen signal (Fig. 8d–f). This oxygen signal is not observed outside of these pores, suggesting that the corrosion is strongly localized to the pores.

Another possibility is that these circular features are blisters of the passivating oxide. First reported by *Bargeron and Givens*, several authors, e.g. *McCafferty and Natishan*, have reported circular, “blisters” of the passivating oxide on pure aluminum in chloride solutions [28–30]. As hydrogen gas is evolved during the pitting corrosion, the pressure inside the pit increases, causing a blister, which can eventually rupture the passivating oxide. Compared to the circular features in the images presented here in Figs. 6–8, the blisters in these previous studies have smoother surfaces. Also, this phenomenon has not previously been published for the AA7xxx alloys. An early paper by *Perkins et al.* reported blistering in dilute Al alloys in seawater [31]. Of the three alloys studied, the closest had a zinc content 6.0–7.4 wt%, 0.005 wt% Cu, and no reported Mg (compared with 5.4Zn-2.25Mg-1.54Cu for AA7075). The blisters described had a hemispherical shape with a smooth surface, unlike the very flat and somewhat pock-marked surfaces of the circular features observed in Figs. 6–8. Further work would be required to determine if the circular features observed on the helium sprayed material are CPZs or blisters.

The He-CS material exhibits the least amount of pitting of the three sample types. As quantified in Table 2, the fraction of surface area comprised of pits after 0.1 M NaCl exposure is greatest for the bulk material. While the nature of the pitting is different between the bulk and the N-CS material, the amount of pitting, quantified as the fraction of the area exposed, is statistically the same. The fraction of pitted area for the He-CS material is measurably less. After the 0.6 M NaCl exposure, the fraction of the surface pitted is much larger for the bulk and N-CS materials than for the He-CS material. However, the fraction of the surface showing generalized corrosion substantially increases with increased chloride concentration.

This initial study on the corrosion behavior of cold sprayed AA7075 strongly suggests that the amount and type of corrosion may be

dominated by the degree of microstructural porosity instead of the amount of plastic deformation in the coating. We have intentionally compared two different cold spray microstructures here: a fully dense, high quality material, sprayed with expensive helium gas; and a less dense, lower quality material sprayed with much less expensive nitrogen gas. The level of plastic deformation in the He-CS material is qualitatively greater than in the N-CS material (high hardness, more clearly deformed particles), and yet the corrosion performance is better. According to work on cold sprayed pure aluminum material [9,10,13], plastic deformation in the coating will enhance the rate of corrosion. While this relationship may be true here as well, the present results suggest that the corrosion response is more strongly controlled by the microstructural porosity. The N-CS material has much greater micro-scale porosity and also has substantially worse corrosion performance, particularly at higher chloride concentrations. This degradation in corrosion performance may be attributed to a form of micro-crevice corrosion based upon the occluded corrosion geometry created by interconnected pores throughout the microstructure of the N-CS material. Further separation of the effects of porosity, plasticity and intermetallics on the corrosion behavior of cold sprayed aluminum alloys will be the topic of a future publication.

4. Conclusion

Here, we reveal the differences in basic corrosion behavior of AA7075 material in bulk, N-CS and He-CS cold spray deposited conditions by utilizing electrochemical and immersion corrosion experimental techniques. Our results suggest that micro-porosity dominates corrosion characteristics and the degree of corrosion. N-CS coatings exhibit limited particle deformation and possess a high degree of resultant porosity, while materials sprayed with helium gas display extensive microstructural deformation and almost no porosity. The He-CS coating exhibits a slightly more active response than the bulk material plate (Fig. 5) for both 0.1 M and 0.6 M NaCl solutions. However, the porous, N-CS coating is substantially more active, particularly in the higher 0.6 M NaCl solution. The nature of localized corrosion is qualitatively different between the three materials with irregular pitting/intergranular corrosion on the bulk material, microscale crevice corrosion on the N-CS coating, and more limited pitting on the He-CS coating. These differences seem to be primarily controlled by microstructural porosity and the distribution of large intermetallic precipitates. It is unclear from the evidence in this study if the distribution of intermetallics along prior particle-cell boundaries has a particularly important influence on the corrosion of the CS coatings material.

Acknowledgements

This research is supported by the ONR-Sea Base Aviation Structures Program under program number: N00014-15-1-2133. SN and GBT also gratefully acknowledge NSF-EPS-0814103. UA's Central Analytical Facility (www.caf.ua.edu) is recognized for additional support and access to the instruments used in this study. We thank Prof. G. Warren for reading and commenting on this manuscript. Finally, we are very grateful for electron microscopy assistance from Mr. T. Liu of UA.

References

- [1] B. Al-Mangour, R. Mongrain, E. Irissou, S. Yue, Improving the strength and corrosion resistance of 316 L stainless steel for biomedical applications using cold spray, *Surf. Coat. Technol.* 216 (2013) 297–307.
- [2] B.S. DeForce, T.J. Eden, J.K. Potter, Cold spray Al-5% Mg coatings for the corrosion protection of magnesium alloys, *J. Therm. Spray Technol.* 20 (2011) 1352–1358.
- [3] F. Gärtner, T. Stoltenhoff, T. Schmidt, H. Kreye, The cold spray process and its potential for industrial applications, *J. Therm. Spray Technol.* 15 (2006) 223–232.
- [4] R. Jones, N. Matthews, R. Green, D. Peng, On the potential of supersonic particle deposition to repair simulated corrosion damage, *Eng. Fract. Mech.* 137 (2015) 26–33.
- [5] K. Ogawa, K. Ito, K. Ichimura, Y. Ichikawa, S. Ohno, N. Onda, Characterization of

- low-pressure cold-sprayed aluminum coatings, *J. Therm. Spray Technol.* 17 (2008) 728–735.
- [6] V.K. Champagne, The repair of magnesium rotorcraft components by cold spray, *J. Fail. Anal. Prev.* 8 (2008) 164–175.
- [7] R. Jones, L. Molent, S. Barter, N. Matthews, D. Tamboli, Supersonic particle deposition as a means for enhancing the structural integrity of aircraft structures, *Int. J. Fatigue* 68 (2014) 260–268.
- [8] S.M. Hassani-Gangaraj, A. Moridi, M. Guagliano, Critical review of corrosion protection by cold spray coatings, *Surf. Eng.* 31 (2015) 803–815.
- [9] J. Karthikeyan, T. Laha, K. Balani, A. Agarwal, N. Munroe, Microstructural and electrochemical characterization of cold-sprayed 1100 aluminum coating, Proceedings of the International Thermal Spray Conference 10–12 May 2004, AMS International: Osaka, 2004, pp. 341–346.
- [10] Y. Tao, T. Xiong, C. Sun, L. Kong, X. Cui, T. Li, G.-l. Song, Microstructure and corrosion performance of a cold sprayed aluminium coating on Az91d magnesium alloy, *Corros. Sci.* 52 (2010) 3191–3197.
- [11] P.S. Pao, S.J. Gill, C.R. Feng, On fatigue crack initiation from corrosion pits in 7075-T7351 aluminum alloy, *Scr. Mater.* 43 (2000) 391–396.
- [12] K.K. Sankaran, R. Perez, K.V. Jata, Effects of pitting corrosion on the fatigue behavior of aluminum alloy 7075-T6: modeling and experimental studies, *Mater. Sci. Eng.: A* 297 (2001) 223–229.
- [13] O. Meydanoglu, B. Jodoin, E.S. Kayali, Microstructure, mechanical properties and corrosion performance of 7075 Al matrix ceramic particle reinforced composite coatings produced by the cold gas dynamic spraying process, *Surf. Coat. Technol.* 235 (2013) 108–116.
- [14] S.C. Morton, G.S. Frankel, Atmospheric pitting corrosion of aa7075-T6 under evaporating droplets with and without inhibitors, *Mater. Corros.* 65 (4) (2014) 351–361.
- [15] R.K. Gupta, M.K. Deschamps, S.P. Lynch, N. Birbilis, Relating the early evolution of microstructure with the electrochemical response and mechanical performance of a Cu-Rich and Cu-Lean 7xxx aluminum alloy, *J. Electrochem. Soc.* 11 (2012) C492–C502.
- [16] O. Molnarova, P. Malk, F. Lukac, T. Chraska, Spark plasma sintering of a gas atomized al7075 alloy: microstructure and properties, *Materials* 9 (2016) 1004.
- [17] M.K. Cavanaugh, R.G. Buchheit, N. Birbilis, Evaluation of a simple microstructural-electrochemical model for corrosion damage accumulation in microstructurally complex aluminum alloys, *Eng. Fract. Mech.* 76 (2009) 641–650.
- [18] R.G. Buchheit, N. Birbilis, Electrochemical microscopy: an approach for understanding localized corrosion in microstructurally complex metallic alloys, *Electrochim. Acta* 55 (2010) 7853–7859.
- [19] R. Ayer, J.Y. Koo, J.W. Steeds, B.K. Park, Microanalytical study of the heterogeneous phases in commercial Al-Zn-Mg-Cu alloys, *Metall. Trans. A* 16 (1985) 1925–1936.
- [20] M. Gao, C.R. Feng, R.P. Wei, An analytical electron microscopy study of constituent particles in commercial 7075-T6 and 2024-T3 alloys, *Metall. Mater. Trans. A* 29 (1998) 1145–1151.
- [21] Y. Liu, J.M.C. Mol, G.C.A.M. Janssen, Combined corrosion and wear of aluminium alloy 7075-T6, *J. Bio- and Triboro-Corros.* 2 (2016) 9.
- [22] S.S. Singh, C. Schwartzstein, J.J. Williams, X. Xiao, F. De Carlo, N. Chawla, 3d microstructural characterization and mechanical properties of constituent particles in Al 7075 alloys using X-ray synchrotron tomography and nanoindentation, *J. Alloys Compd.* 602 (2014) 163–174.
- [23] X. Guo, G. Zhang, W. Li, Y. Gao, H. Liao, C. Coddet, Investigation of the microstructure and tribological behavior of cold-sprayed Tin-bronze-based composite coatings, *Appl. Surf. Sci.* 255 (2009) 3822–3828.
- [24] B. Jodoin, L. Ajdelstajn, E. Sansoucy, A. Zúñiga, P. Richer, E.J. Lavernia, Effect of particle size, morphology, and hardness on cold gas dynamic sprayed aluminum alloy coatings, *Surf. Coat. Technol.* 201 (2006) 3422–3429.
- [25] V.T. Steenkiste, J.R. Smith, C. Moreau, B. Marple (Eds.), *Evaluation of Coating Produced Via Kinetic and Cold Spray*, in: *Thermal Spray 2003: Advancing the Science, Applying the Technology*, ASM International, Materials Park, OH, USA, 2003, pp. 53–61.
- [26] D.L. Gilmore, R.C. Dykhuizen, R.A. Neiser, T.J. Roemer, M.F. Smith, Particle velocity and deposition efficiency in the cold spray process, *J. Therm. Spray Technol.* 8 (1999) 576–582.
- [27] O.C. Ozdemir, C.A. Widener, D. Helfritch, F. Delfanian, Estimating the effect of helium and nitrogen mixing on deposition efficiency in cold spray, *J. Therm. Spray Technol.* 25 (2016) 660–671.
- [28] P.M. Natishan, E. McCafferty, The mechanism of blister formation and rupture in the pitting of ion-implanted aluminum, *J. Electrochem. Soc.* 136 (1) (1989) 53–58.
- [29] E. McCafferty, Sequence of steps in the pitting of aluminum by chloride ions, *Corros. Sci.* 45 (2003) 1421–1438.
- [30] C.B. Bargeron, R.B. Givens, Precursive blistering in the localized corrosion of aluminum, *Corrosion* 36 (11) (1980) 618–625.
- [31] J. Perkins, J.R. Cummings, K.J. Graham, Morphological studies of occluded cells in the pitting of dilute aluminum alloys in seawater, *J. Electrochem. Soc.* 129 (1) (1982) 137–141.